



Structural and thermoelectric characterization of Ba substituted LaCoO_3 perovskite-type materials obtained by polymerized gel combustion method

Robert Kun ^{a,*}, Sascha Populoh ^b, Lassi Karvonen ^b, Julia Gumbert ^a, Anke Weidenkaff ^b, Matthias Busse ^{a,c}

^a University of Bremen, FB 4, Near Net Shape Technologies, Wiener Str. 12, 28359 Bremen, Germany

^b Solid State Chemistry and Catalysis, EMPA, Swiss Federal Laboratories for Materials Science and Technology, Ueberlandstrasse 129, CH-8600 Duebendorf, Switzerland

^c Fraunhofer Institute for Manufacturing Technology and Applied Materials Research, IFAM, Wiener Str. 12, 28359 Bremen, Germany



ARTICLE INFO

Article history:

Received 8 February 2013

Received in revised form 21 April 2013

Accepted 4 May 2013

Available online 16 May 2013

Keywords:

Thermoelectric

Oxide materials

Barium ion

La-cobaltate

Chimie douce

ABSTRACT

Structural and thermoelectric transport properties of Ba^{2+} containing lanthanum cobaltate ($\text{La}_{1-x}\text{Ba}_x\text{CoO}_3$; $x = 0.01, 0.03, 0.05$) prepared by soft chemistry method were investigated and discussed. The influence of the fuel-to-oxidizer ratio (Φ) of the redox mixture on the powder microstructure was studied. The agglomeration grade of the nanocrystalline perovskite phases can be influenced due to initial composition of the redox mixture. Since the different burning characteristic of the polymerized gels results in different xerogel structures, the as-calcined single phase perovskite samples show different compacting and sintering behavior. The thermoelectric transport properties were measured in the 300–1300 K temperature range. It was found that the electrical and thermal conductivity of the sintered pellets show strong dependence on microstructure. In addition increasing Ba^{2+} content in the samples results in lower thermal conductivity values ($\kappa < 1.5 \text{ W/K m}$). The calculated dimensionless figure of merit (ZT) showed maximum value in the 400–500 K range.

© 2013 Elsevier B.V. All rights reserved.

1. Introduction

Nowadays, thermoelectric energy conversion is becoming more important, since it provides the possibility of environmentally clean, scalable power generation from otherwise unused waste heat. Thermoelectric generators consisting of n- and p-type semiconductor legs connected electrically in series and thermally in parallel are solid state, low maintenance and durable devices. The direct conversion of the heat into electricity by thermoelectric materials is based on the Seebeck-effect. The efficiency of a thermoelectric material can be expressed by the dimensionless figure-of-merit (ZT), which is defined as $\text{ZT} = S^2 T \sigma / \kappa$, where S , σ , T and κ are the Seebeck coefficient, electrical conductivity, absolute temperature and thermal conductivity, respectively. In general, efficient thermoelectric material exhibits large absolute Seebeck coefficient (S), high electrical conductivity (σ) and at the same time low thermal conductivity (κ). Up to now, $\text{ZT} = 1$ rates as a typical benchmark value and the strong interdependence of S , σ and κ makes the ZT enhancement especially difficult [1–3]. Authors have reported ZT values beyond the benchmark value for nanostructured materials, where the enhanced ZT value was realized primarily due to decreased thermal conductivity [3,4]. Thermal

conductivity (κ_{total}) in metals and semiconductors can be discussed in terms of electronic (κ_e) and phonon (κ_{ph}) contribution, $\kappa_{\text{total}} = \kappa_e + \kappa_{\text{ph}}$. While in metals the electronic contribution to the overall thermal conductivity is predominant, in semiconductors the majority of heat is transported by phonons (i.e. collective lattice vibrations).

Perovskite type cobaltates are promising thermoelectric oxides [5]. Substitution of La^{3+} by divalent ions in LaCoO_3 , such as Ca^{2+} , Sr^{2+} , Ba^{2+} has a significant influence on the spin state of $\text{Co}^{3+}/\text{Co}^{4+}$, oxygen vacancy concentration and/or crystal-structure distortions in the material, which also affect the physical, i.e. electric and magnetic properties [6,7]. For instance, substitution of La^{3+} with Ba^{2+} results in enhanced oxide ion conductivity in the samples up to certain Ba^{2+} levels [8]. It was reported earlier that electrical conductivity of $\text{La}_{1-x}\text{Ba}_x\text{CoO}_3$ shows unusual behavior due to high temperature semiconductor–metal transition at low doping (x) levels, or changing from semiconductor to metal at higher ($x \approx 0.50$) doping levels [9]. Previous studies showed that semiconductor–metal transition takes place at about $x \sim 0.20$ doping levels in $\text{La}_{1-x}\text{Ba}_x\text{CoO}_3$ and in the same time above this level the samples display ferromagnetic metal behavior [10].

Over the years several wet chemical synthesis methods have been proposed and developed for preparation of oxide ceramics. Notable methods are sol-gel [11], Pechini-method or so-called polymerized citrate complex method [12,13], co-precipitation

* Corresponding author. Tel.: +49 4212246353; fax: +49 4212246300.
E-mail address: robert.kun@uni-bremen.de (R. Kun).

[14,15], microemulsion mediated [16] and hydro/solvothermal method [17].

In the present study Ba^{2+} doped LaCoO_3 ceramics were prepared by means of gel combustion method and characterized for their thermoelectric transport properties. The effect of the fuel-to-oxidizer ratio on the crystal and micro structure of the as-prepared perovskite powders as well as of the sintered pellets was studied. Thermoelectric transport properties were determined in the 300–1300 K temperature range. Relationship between the gel combustion characteristics, powder microstructure and sinterability, as well as thermoelectric transport properties are discussed in detail.

2. Experimental

2.1. Material preparation

In this study a series of four samples was synthesized. The sample labels, composition and the applied fuel-to-oxidizer ratio are summarized in Table 1. In order to obtain $\text{La}_{1-x}\text{Ba}_x\text{CoO}_3$ ($0.01 \leq x \leq 0.05$) samples corresponding high purity metal nitrates (Sigma-Aldrich, $\text{La}(\text{NO}_3)_3 \cdot 6 \text{H}_2\text{O}$, $\text{Co}(\text{NO}_3)_2 \cdot 6 \text{H}_2\text{O}$, $\text{Ba}(\text{NO}_3)_2$) were used as source materials. Analytical grade L-malic acid (MA) (Sigma-Aldrich, $\text{C}_4\text{H}_6\text{O}_5$, anhydrous, $\geq 99.5\%$) was used as chelating agent (and fuel) and ethylene glycol (EG) (Fluka, $\text{C}_2\text{H}_6\text{O}_2$, $\geq 99.5\%$) was applied for promoting polyetherification. The calculated amounts of metal salts were dissolved first in deionized water followed by the mixing of malic acid solution. To provide highest gel homogeneity and avoid impurities due to precipitation malic acid was used as fuel during syntheses instead of citric acid, which latter is well known from the so-called *citrate-nitrate gel method*. The molar ratio of total metal ion (Me) to the malic acid was adjusted to 1:3. The pH of the solution was measured to pH 1 (at $T = 298$ K). The metal ion-malic acid solution was stirred for 2 h at 333 K then calculated amount of ethylene glycol (MA:EG = 1:2) was added drop wise to the stirred complex solution. A sample (labeled as LBCO1) with reduced organic content (i.e. decreased fuel-to-oxidizer ratio, Φ) was also prepared, where $\Sigma\text{Me:MA:EG} = 1:1:1$. Subsequently temperature of the reaction system was raised to 363 K to promote polyetherification between hydroxyl- and carboxylic groups of ethylene glycol and malic acid, respectively. Due to elevated temperature the solution medium was evaporated within 4–5 h and a high viscous purple colored, homogeneous gel was obtained. It should be noted, no precipitation was observed during *polymeric gel formation*. The viscous gels were afterwards decomposed under air at 473 K ignition temperature in hot box oven. The auto combustion took place within 40 min and voluminous, brownish *xerogels* were obtained. The xerogels were then fully grounded in agate mortar and calcined at 973 K for 6 h under air, resulting in shiny black powders. For the characterization of the thermoelectric transport properties, the calcined powders were pelletized into disks under uniaxial pressure at 151 MPa, and the pellets were sintered at 1473 K for 2 h for two times in muffle furnace under air; 5 K/min heating rate was applied each time.

2.2. Characterization methods

Thermoanalytical measurements (TG, DTA) were performed by Derivatograph MOM Q-1500 D instrument in dynamic mode under static air. The xerogel samples (~ 100 mg each) were heated in ceramic crucibles from room temperature to 1273 K applying 5 K/min heating rate. Each sample was measured against mass-stable $\alpha\text{-Al}_2\text{O}_3$ reference.

FT-IR spectra of the xerogels were recorded by Bruker Equinox 55 spectrometer in the 4000–650 cm^{-1} range in ATR mode using diamond window. The number of background and sample scans was 128 each with a resolution of 4 cm^{-1} .

The phase purity and the crystal structure of the calcined compounds were investigated by powder X-ray diffraction (XRD). XRD data were collected on a PAN-analytical X'Pert Pro $\theta\text{-}\theta$ diffractometer, equipped with a linear detector (X'Celerator) and $\text{Cu K}\alpha_1$ radiation. The following setting in primary beam direction

was used: a graphite-monochromator, a divergence slit $1/2$, a 10 mm mask; a divergence slit $1/4$ and a Ni-filter. Step scanning mode with a scan speed of 0.01°/s over a 2θ range of $0^\circ \leq 2\theta \leq 140^\circ$ was applied. The refinement of the crystal structures was performed by the Rietveld method, using BRASS (Bremen Rietveld Analysis and Structure Suite, version 2.2.0 26.05.2011 established by ZEKAM, i.e. "Zentrallabor für Kristallographie und Angewandte Materialwissenschaften" University of Bremen). In order to fit the calculated values from the structure model (y_c) into the measured data (y_o), a spline-interpolation polynomial function was used as a background model and a split pseudo Voigt function as peak shape model.

Crystallite size of the polycrystalline powders were characterized by Tecnai F20 S-Twin transmission electron microscope (TEM). Scanning electron micrographs and elementary composition of calcined powders as well as of sintered pellets were taken by FEI Helios NanoLab™ 600 DualBeam™ system equipped with an Oxford X-Max 80 energy dispersive X-ray SD-Detector (EDX).

The thermal conductivity of the samples was measured indirectly by measurements of the thermal diffusivity α (Netzsch LFA 457 Microflash) on disc shaped sintered samples, and of the specific heat C_p (Netzsch DSC 404 C). The density of the porous samples was determined from geometry and mass determination. Subsequently, the electrical conductivity and the Seebeck coefficient were determined by using RZ2001i Ozawa Science measurement system (Ozawa Science Co., Nagoya, Japan) on $1.5 \times 1.5 \times 8 \text{ mm}^3$, bar shaped samples cut out from the sintered pellets.

3. Results and discussion

The thermal behavior of the as-prepared xerogels was investigated by thermoanalytical methods. In Fig. 1a the TG curves of LBCO samples are presented. The whole decomposition process can be divided into four regions. About 5–8% weight loss occurs in the first section, followed by the most pronounced weight loss in the second thermal regime, which is common to all our xerogel samples. In the third region slight weight losses were registered and through the fourth section the samples were mass stable. Conspicuously, the total maximum weight loss up to 873 K in the case of LBCO1, with a reduced fuel-to-oxidizer ratio, is smaller (about 50%) as compared to the other samples (about 75%). This observation can be explained with the different combustion characteristics of the polymeric gels. Based on the propellant chemistry principle [18] the heat of combustion (i.e. exothermicity of the redox reaction) is the highest when the ratio of the net reducing valence of fuel to the net oxidizing valence of metal nitrates tends to unity. In other words the fuel-to-oxidizer ratio (Φ) should be 1. In the present study malic acid and ethylene glycol acted as fuel and metal nitrates as oxidizer during the combustion reaction. Detailed description of calculation of fuel-to-oxidizer ratio was reported previously elsewhere [19]. In the case of LBCO1 the calculated Φ was 1.7, and for LBCO1a/1b/1c it was around 7.7. Nevertheless, both compositions correspond to fuel-rich conditions.

The DTA curves (Fig. 1b) were recorded in parallel to TG measurements. The above mentioned decomposition steps can be recognized as endothermic and exothermic peaks. In the first (298–473 K) section an endothermic peak can be seen which can be attributed to the elimination of the physically adsorbed water. In the second thermal regime (473–773 K) several exothermic peaks can be observed, where the residual nitrates and organics as well as carbonaceous by-products leave the xerogels [20]. In the case of LBCO1 sample the main exothermic peak in the DTA curve can

Table 1

Fuel-to-oxidizer ratio, chemical composition and comparison of the measured and calculated thermal conductivity values of the samples.

Sample name	Fuel-to-oxidizer ratio (Φ) ^a	Theoretical Ba^{2+} content (at.%)	Practical Ba^{2+} content (at.%) ^b	Measured thermal conductivity ^c κ [W/m K]	Porosity	Corrected thermal conductivity ^d κ_0 [W/m K]
LBCO1	1.7	1	0.91 ± 0.09	2.06	0.088	2.26
LBCO1a	7.7	1	0.97 ± 0.09	0.65	0.361	1.02
LBCO1b	7.7	3	2.75 ± 0.10	0.48	0.381	0.78
LBCO1c	7.7	5	4.96 ± 0.22	0.49	0.397	0.81

^a calculated using the formulae found in Ref. [19].

^b determined by EDX analysis, see details in Section 2.

^c experimental data measured at $T = 373$ K.

^d calculated by Eq. (1).

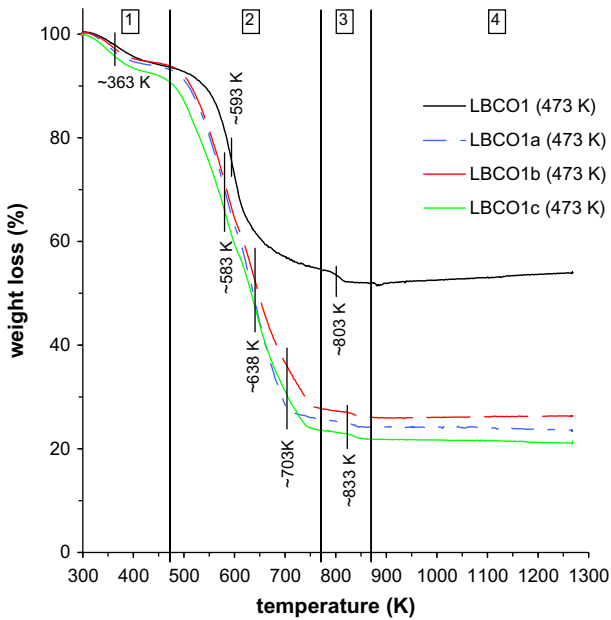


Fig. 1a. Thermogravimetric (TG) analyses of the as-prepared xerogels.

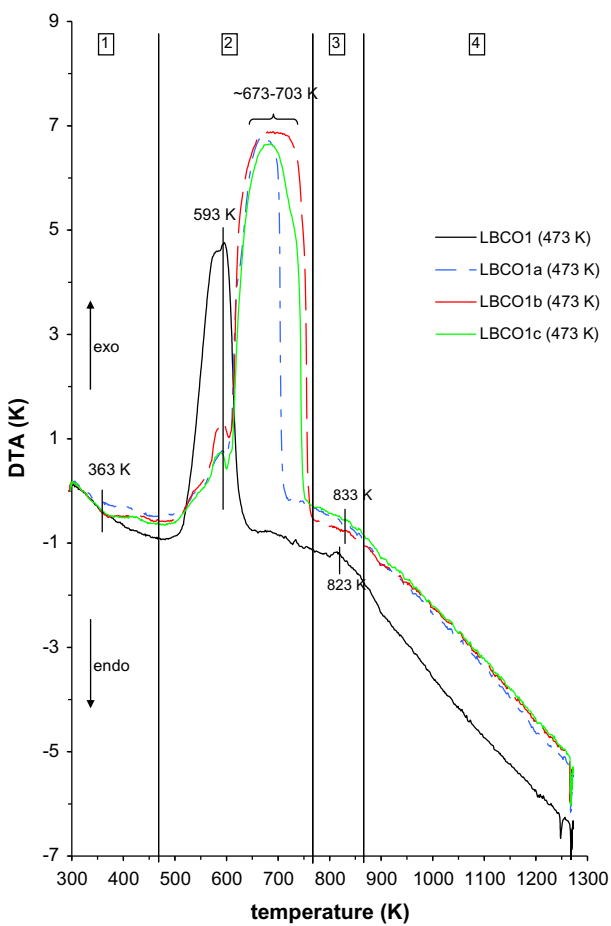


Fig. 1b. Differential thermal analysis (DTA) curves of the LBCO xerogels.

be found at about 593 K. Supposedly in this peak two main thermal processes are overlap, therefore this temperature difference could be recorded as the sum of the released heat due to (i) decomposition

of residual nitrate ions and (ii) oxidizing of the residual organics [21]. In case of the samples LBCO1a, 1b, 1c a smaller exothermic peak can be found at 593 K and a broad exothermic peak appears at around 673–703 K. In the LBCO1 gel the relatively higher amount of nitrate compared to the organics may promote the elimination of the organics and/or carbonaceous combustion by-products leading to an effective oxidation already at lower temperatures. In contrast to that, in case of polymeric gels prepared with higher Φ the relative amount of nitrate is less. Consequently the same auto-combusted gel contains significant amount of non-reacted and/or partially combusted organics (see corresponding weight losses in Fig. 1a) which will then be oxidized at higher temperatures. As a result, the decomposition of polymeric gels prepared with higher Φ is eventuated in two separate exothermic events. Associated with the slight weight losses in the third thermal regime (773–873 K), diminutive exothermic signals were detected in the DTA curves (Fig. 1b). At this temperature region the decomposition of the possibly present metal- and other carbonate species can take place [13]. However, the presence of such carbonate compounds was not evidenced in any of the as-prepared xerogels. Finally, in the fourth region (873–1273 K) no thermal event was registered.

The differences in the chemical composition and nature of as-prepared xerogels were further analyzed by FT-IR ATR spectroscopy. In Fig. 2 the corresponding spectra are shown. The broad absorption band at around 3250 cm^{-1} is characteristic of stretching vibration of hydroxyl group ($\nu(\text{O}-\text{H})$). The band found at around 2940 cm^{-1} in the spectra of LBCO1a, 1b, 1c relates to asymmetrical stretching vibration of $(-\text{CH}_2-)$ group [22], and the band at 2342 cm^{-1} originates from presenting CO_2 . The band below 700 cm^{-1} could originate from metal–oxygen (M–O) bonds [23,24]. The major differences between the FT-IR spectra of LBCO1 ($\Phi = 1.7$) and the other three samples ($\Phi = 7.7$) can be observed in the $1800\text{--}700\text{ cm}^{-1}$ spectral range. In case of the LBCO1 xerogel significantly less absorption bands were assigned, which suggest a more complete decomposition of polymeric resin during the autocombustion process. Accordingly, the absorption band appears at 833 cm^{-1} is characteristic of nitrate anion, however the peaks at about 780 cm^{-1} and 1375 cm^{-1} could originate from stretching vibration of $(-\text{C}=\text{O})$ related to carboxylate group or from nitrate anion, as well [25]. Peak found at 1557 cm^{-1} and the slight shoulder observed at around 1634 cm^{-1} are attributed to the asymmetrical stretching vibration of carboxylate anion and carbonyl group, respectively, which is a clear indication of organic matter presents in the as-prepared xerogel. In the FT-IR absorption spectra of the LBCO1a, 1b and 1c xerogels several other bands can also be found. Peaks at 864 cm^{-1} and 970 cm^{-1} are attributable to vibrations of CH groups ($\gamma(\text{CH})$) and the absorption bands at 1030 cm^{-1} and 1082 cm^{-1} are characteristic of symmetrical stretching vibration of $\text{C}=\text{O}(\text{H})$ groups. The sharp peak located at 1155 cm^{-1} and the following bands at 1244 cm^{-1} and at 1275 cm^{-1} can be attributed to asymmetrical stretching of $\text{C}=\text{O}-\text{C}$ bond which chemically derived from the carboxylic acid ester functional group. The band at 1425 cm^{-1} which appears as a shoulder in the spectra, is related to the symmetrical bending vibration of $-\text{CH}_2-$ ($\delta_s\text{CH}_2$) group in the form of $(-\text{CO}-\text{CH}_2-)$ bond, whose existence can be explained by the presence of pristine or partially decomposed malic acid. The sharp band appeared at about 1717 cm^{-1} can be associated with symmetrical stretching vibration of $(-\text{C}=\text{O})$ originate from ester-, or carboxylic functional group [26].

In Fig. 3 the powder XRD patterns of calcined Ba^{2+} doped $\text{La}_{1-x}\text{Ba}_x\text{CoO}_3$ ($0 \leq x \leq 0.05$) perovskite cobaltates ($\Phi = 1.7$ for $x = 0.01$, and $\Phi = 7.7$) are shown in the $20^\circ \leq 2\theta \leq 80^\circ$ range. The patterns of the samples prepared with $\Phi = 7.7$ have similar intensities, however the sample prepared with $\Phi = 1.7$ shows higher intensities with same intensity ratio as the other ones. The splitting of the reflections (110) and (104) at $2\theta \approx 32.9^\circ$ and $2\theta \approx 33.2^\circ$ (see

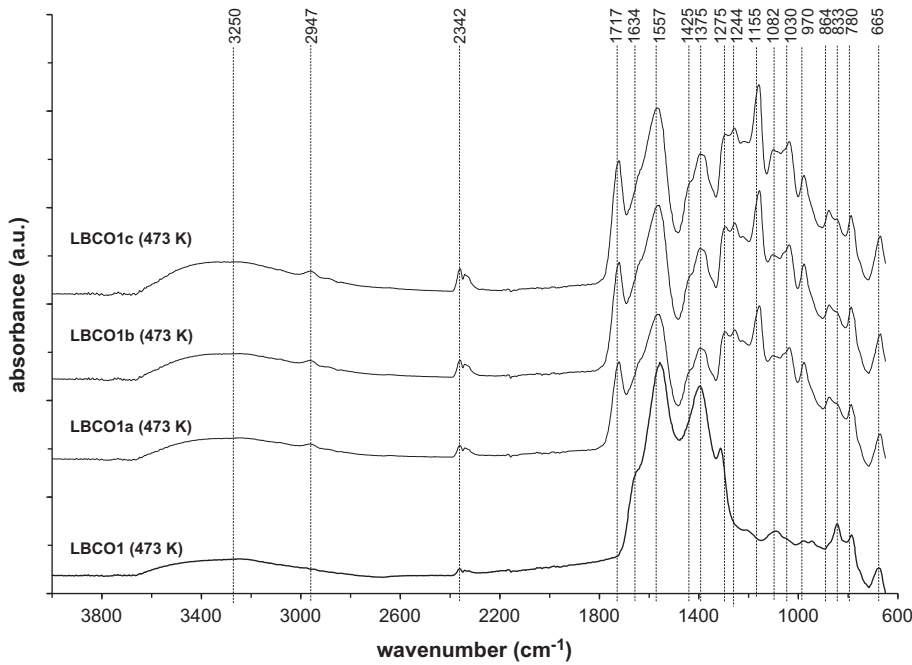


Fig. 2. Fourier transform IR-ATR spectra of the as-prepared xerogels.

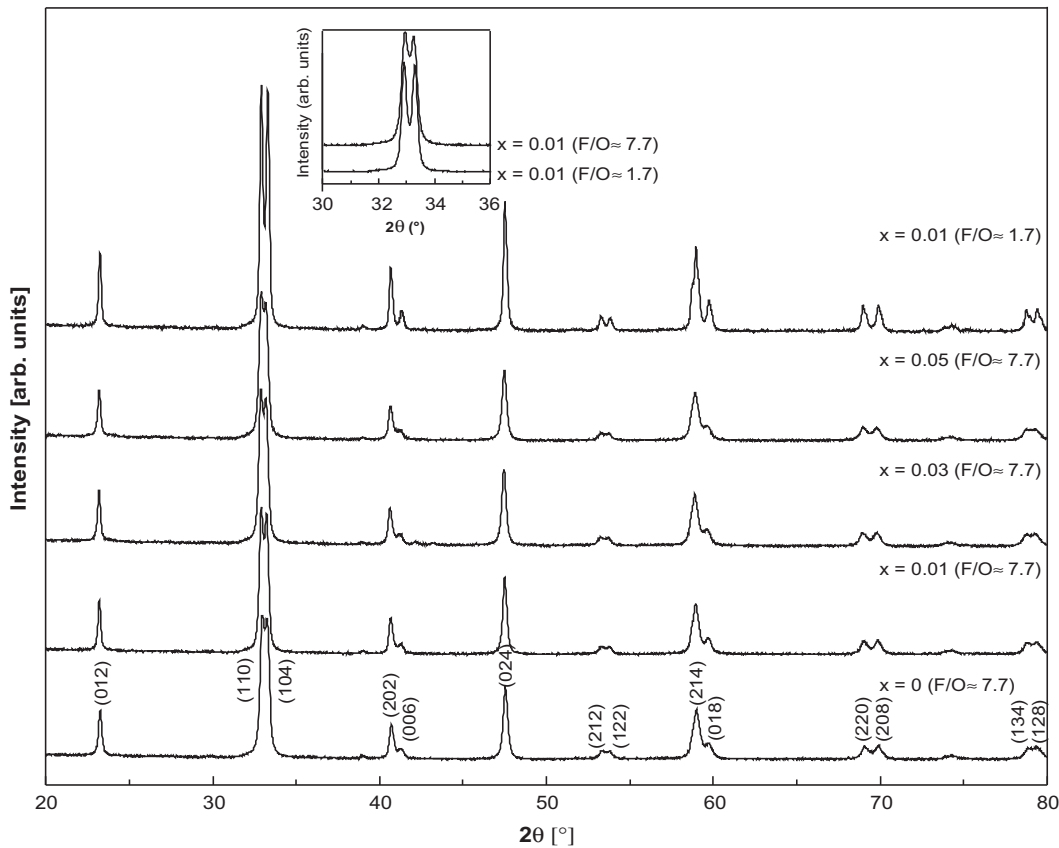


Fig. 3. Powder XRD patterns of Ba^{2+} doped $\text{La}_{1-x}\text{Ba}_x\text{CoO}_3$ (with $0 \leq x \leq 0.05$) compounds.

inset picture) is better visible by the sample with lower Φ due to narrower reflection profile caused by bigger crystallite size. All samples crystallize in single phase and can be indexed in the rhombohedral symmetry with space group R-3c (space group number #167 of the *International Tables for Crystallography* (ITC)) having

lattice parameters of approximately $a_p\sqrt{2} \times a_p\sqrt{2} \times 2a_p\sqrt{3}$, $\gamma = 120^\circ$ (hexagonal setting), where $a_p \approx 3.8 \text{ \AA}$ corresponds to the ideal cubic perovskite lattice parameter. In the R-3c space group the atoms are located at M=La, Ba (0, 0, $\frac{1}{4}$), Co (0, 0, 0) and O (x , 0 , $\frac{1}{4}$), with $x = 0.5$ for the parent LaCoO_3 phase and $x \approx 0.5$ for

Table 2Rietveld refined structural parameters for Ba^{2+} doped $\text{La}_{1-x}\text{Ba}_x\text{CoO}_3$ ($0 \leq x \leq 0.05$) perovskites.

Compounds	$x = 0$	$x = 0.01$	$x = 0.03$	$x = 0.05$	$x = 0.01$
Crystal system space group	Rhombohedral R 3 –				
	$c=167$; $\alpha = \beta = 90^\circ$; $\gamma = 120^\circ$				
	$\Phi = 1.7$				$\Phi = 7.7$
<i>Lattice parameters</i>					
$a = b$ (Å)	5.436 (4)	5.438 (4)	5.440 (4)	5.441 (4)	5.442 (5)
c (Å)	13.132 (4)	13.126 (4)	13.140 (4)	13.145 (4)	13.108 (4)
Cell volume (Å ³)	336.07(2)	336.15 (2)	336.76 (2)	336.97 (2)	336.15 (2)
$M = \text{La, Ba}$	6a ^a				
x	0.0000	0.0000	0.0000	0.0000	0.0000
y	0.0000	0.0000	0.0000	0.0000	0.0000
z	0.2500	0.2500	0.2500	0.2500	0.2500
B_{iso} (Å ²)	0.56 (2)	0.47 (2)	0.74 (2)	0.74 (2)	0.68 (2)
Co	6b ^b				
x	0.0000	0.0000	0.0000	0.0000	0.0000
y	0.0000	0.0000	0.0000	0.0000	0.0000
z	0.0000	0.0000	0.0000	0.0000	0.0000
B_{iso} (Å ²)	0.43 (2)	0.60 ^b	0.30 (2)	0.36(2)	0.25 (2)
O	18a ^a				
x	0.4537 (3)	0.4549 (3)	0.4488 (3)	0.4601 (3)	0.4554 (3)
y	0.0000	0.0000	0.0000	0.0000	0.0000
z	0.2500	0.2500	0.2500	0.2500	0.2500
B_{iso} (Å ²)	1.34 (1)	1.86 (2)	1.33 (1)	2.47 (1)	1.86(1)
R-factors (%)					
R_p	2.22	2.13	2.19	2.06	1.95
R_{wp}	2.93	2.75	2.94	2.65	2.49
R_{Bragg}	4.29	4.77	3.67	4.05	3.65
<i>Bond length</i> (Å)					
Co–O	1.930 (3)	1.929 (3)	1.932 (3)	1.927 (3)	1.929 (3)
<i>Bond angles</i> (°)					
Co–O–Co	165.00 (1)	165.40 (1)	164.36 (1)	167.07 (1)	165.55 (1)

^a Atoms are located at the following Wyckoff positions.^b After refinement B shows for Co a negative value. Therefore B was fixed (standard deviation is given in brackets).

Ba^{2+} substituted phases [27–29], similarly as reported for the $\text{La}_{1-x}\text{Cd}_x\text{CoO}_3$ system [30].

The unrefined XRD patterns of the Ba^{2+} doped $\text{La}_{1-x}\text{Ba}_x\text{CoO}_3$ phases ($0 \leq x \leq 0.05$, $\Phi \approx 7.7$) have the same peak intensities, while the Ba^{2+} substituted LaCoO_3 phase with $x = 0.01$ with less $\Phi \approx 1.7$ has higher peak intensities, with same intensity-ratio (at same measurement conditions). Especially the main reflections at $2\theta \approx 32.9^\circ$ ($1\ 1\ 0$) and $2\theta \approx 33.2^\circ$ ($1\ 0\ 4$) show stronger splitting at low Φ .

Because of the similar scattering factors (s_{fac}) of La^{3+} and Ba^{2+} , the structure factor is not largely affected by Ba^{2+} substitution, explaining the similar relative reflection intensities for all Ba^{2+} doped LaCoO_3 phases with $\Phi = 7.7$. Higher intensities with smaller “Full width at half maximum” (FWHM) of the Ba^{2+} doped phase at $x = 0.01$, $\Phi \approx 1.7$ result from bigger crystallite size (crystallites in the order of 100–120 nm) compared to the Ba^{2+} doped phase prepared at $\Phi = 7.7$ (crystallites in the order of 50–80 nm and broader reflections).

The structural parameters were refined using the Rietveld method, see Table 2. The higher and well-marked intensities for Ba^{2+} doped $\text{La}_{1-x}\text{Ba}_x\text{CoO}_3$ at $x = 0.01$, $\Phi = 1.7$ show the best profile fit, indicated by the good agreement between y_o and y_c for all samples and the small profile R-factors R_p and R_{wp} . The intensity fit for all samples shows good fit as seen in small R_{Bragg} values. The lattice parameters and the calculated cell volume for all compositions are shown in Fig. 4 as a function of Ba^{2+} content. Homogeneous random and solid solutions usually obey the Vegard's law, i.e. composition and structural parameters linearly depend on each other [31].

The expansion of the unit cell volume (Å³) and the increase of cell parameters with progressive Ba^{2+} doping ($0 \leq x \leq 0.05$) are

attributed to the substitution effect in which La^{3+} (1.36 Å [CN:12]) ions are replaced by bigger sized Ba^{2+} (1.61 Å [CN:12]) ions [32]. The compositional parameter x increases simultaneously to the lattice parameters. The deformation of the rhombohedral unit cell shows anisotropic effects, which is seen in the refined lattice parameters. The parameter $a = b$ for the Ba^{2+} doped LaCoO_3 -system with $\Phi = 7.7$ increases smoothly with increasing Ba^{2+} . The lattice parameter ($a = b$) for the Ba^{2+} substitutions level of $x = 0.01$ with $\Phi = 1.7$ increases more than the maximum Ba^{2+}

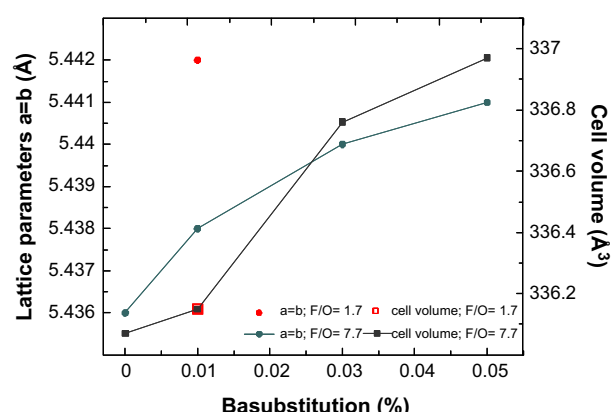


Fig. 4. Ba^{2+} substitution and fuel-to-oxidizer ratio dependences of lattice parameter $a = b$ and cell volume of Ba^{2+} doped $\text{La}_{1-x}\text{Ba}_x\text{CoO}_3$ ($0 \leq x \leq 0.05$) as a function of Ba^{2+} content.

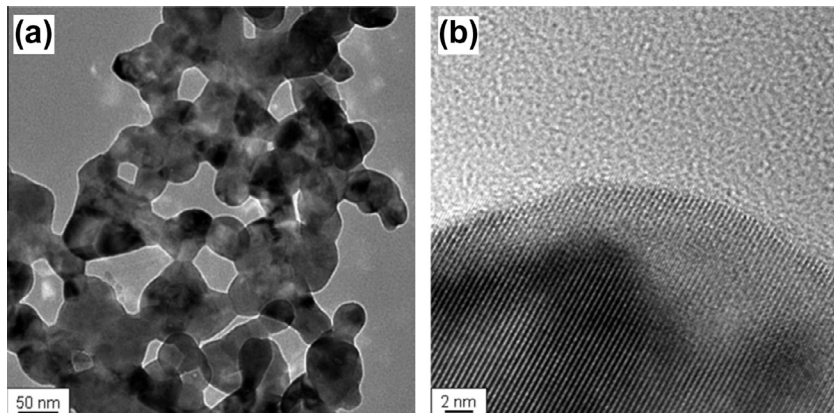


Fig. 5. TEM (a) and HR-TEM (b) micrographs of the calcined LBCO1 perovskite sample.

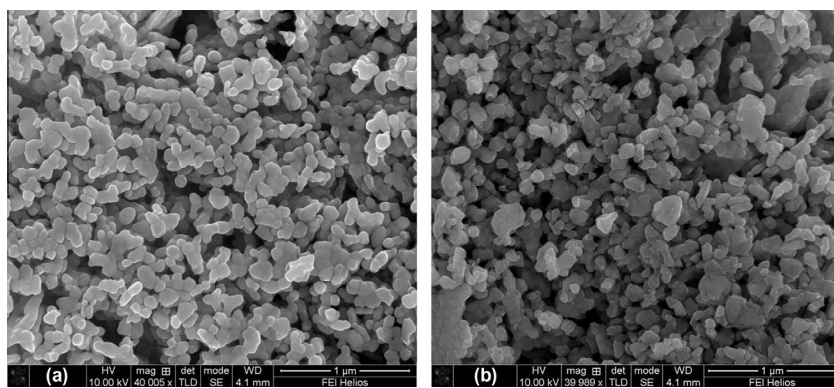


Fig. 6. Scanning electron microscopy images of the calcined (973 K/6 h) LBCO perovskite phases, (a) LBCO1, (b) LBCO1a.

doped $x = 0.05$ sample with $\Phi = 7.7$, but the lattice parameter c decreases to values below the lattice parameter of the pure LaCoO_3 phase. The assumption of anisotropic lattice parameter effects is strengthened by a same unit cell volume of the same Ba^{2+} substitutions level $x = 0.01$ of both fuel-to-oxidizer ratios. Therefore its understood that in LBCO1 sample Ba^{2+} -ions occupy different A-sites in the ABO_3 structure than in LBCO1a sample, generating an anisotropic lattice parameter effect. This depends on the chosen Φ , which shows a direct relation to the reaction time during the crystal growth, which is directly linked to the arrangement of the replacing Ba^{2+} ions in the lattice. Hence the rhombohedral distortion increases (as evidenced by the increasing cell volume and increasing lattice parameter). These are connected to the substitution of La^{3+} by Ba^{2+} due to the increased amount of larger sized Ba^{2+} , compared to the pure LaCoO_3 phase.

A decreasing trend of the $\text{Co}-\text{O}$ bond length and an increasing trend in the $\text{Co}-\text{O}-\text{Co}$ bond angles are ascertained, see Table 2. Except $\text{La}_{1-x}\text{Ba}_x\text{CoO}_3$ ($\Phi = 7.7$, $x = 0.03$) the bond length is larger and the bond angle is smaller compared to the pure LaCoO_3 phase. It was observed for the Ba^{2+} doped phase ($x = 0.01$) that values of the $\text{Co}-\text{O}$ bond lengths for both fuel-to-oxidizer ratios were the same and the $\text{Co}-\text{O}-\text{Co}$ bond angles showed similar values.

Substitution of A-site La^{3+} by Ba^{2+} results in a formation of electronic (creation of mixed valency ($\text{Co}^{3+}-\text{Co}^{4+}$)) and/or ionic defects (creation of oxygen vacancies), latter results in a reduction of cell volume. Due to increasing cell volume (for both Φ values and with increasing Ba^{2+} content, as well) and calculated bond length, it was inferred from Rietveld refinements that charge compensation originates mainly from electronic defects (i.e. created

mixed valency of Co^{3+} and Co^{4+}), rather than oxygen vacancies (see Table 2). However, it cannot be ruled out that a combination of mixed valency and oxygen vacancies exist, but A-site substitution seems to be more determined by Co oxidation than oxygen deficiency [33].

The transition from low spin (LS) state to high spin (HS) state in the parent LaCoO_3 system is a function of temperature. We assume that larger orbital spread is preferred and the Co^{3+} exist in high spin (HS) state, due to increasing cell volume through bigger sized Ba^{2+} ions. On the other hand the Co^{4+} (0.53 Å [CN:6]) with smaller ionic radius than for Co^{3+} (0.61 Å [CN:6]) ionic radius squeezes the $\text{Co}-\text{O}$ bond length (range of interatomic distances: $\text{Co}^{3+}(\text{HS}), \text{Co}^{4+}(-\text{HS})-\text{O} = 2.01-1.93$ Å [32]. Comparison to our data suggests that the Co^{4+} LS ions (energetically favorable, the ionic radius for Co^{4+} LS is not defined, but must be smaller than the Co^{4+} HS state ion) are more dominant in the crystal structure, because the $\text{Co}-\text{O}$ bond length shows for the Ba^{2+} doped samples an overall trend to shorter $\text{Co}^{4+}(\text{LS})-\text{O}$ bond length.

In Fig. 5 TEM images of $\text{La}_{1-x}\text{Ba}_x\text{CoO}_3$ are presented. Generally, the polycrystalline perovskite samples obtained from gel combustion reaction followed by calcination at 973 K have an average primary particle size of 50–80 nm. On the HRTEM image (Fig. 5b) a highly crystalline particle with ordered lattice fringes can be seen.

Some typical SEM images taken from LBCO samples are shown in Fig. 6a and b. Sample prepared with lower Φ (LBCO1; Fig. 6a) disposes of slightly larger primary crystallite size than that of samples prepared at higher Φ (e.g. LBCO1a, see Fig. 6b). At constant Φ but with increasing Ba^{2+} content no considerable differences in primary crystallite size can be observed.

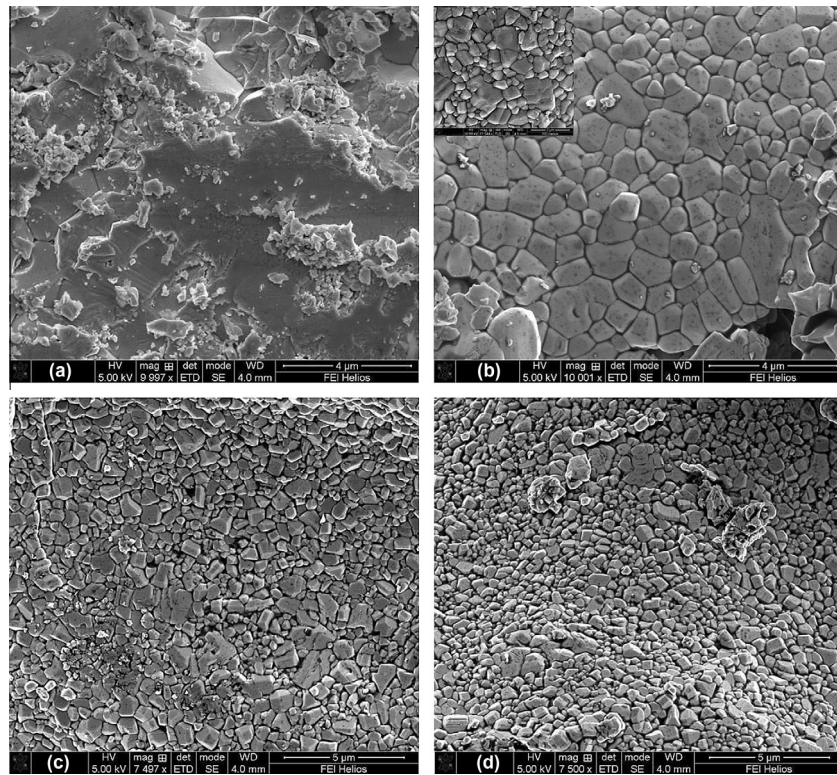


Fig. 7. Cross sectional SEM images of the sintered (1473 K/2 h) LBCO pellets, (a) LBCO1, (b) LBCO1a, (c) LBCO1b, (d) LBCO1c.

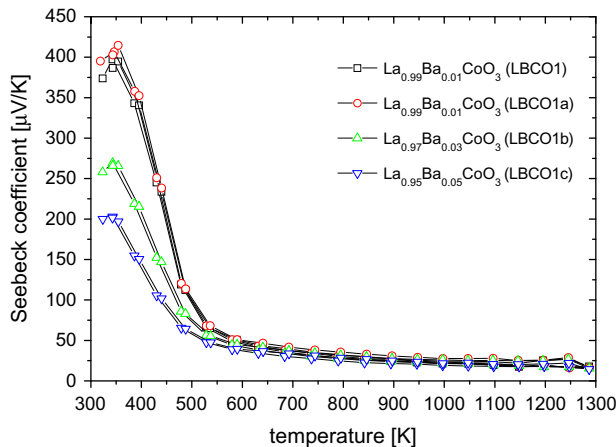


Fig. 8a. Temperature dependence of the Seebeck coefficients (S) for the $\text{La}_{1-x}\text{Ba}_x\text{CoO}_3$ ($0.01 \leq x \leq 0.05$) samples.

In Fig. 7a–d cross sectional SEM images taken from cutting surface of the sintered pellets are presented. In the Fig. 7a the LBCO1 sample shows high compactness and less grain boundaries can be observed. The density of this probe determined from the geometry and mass is 6.7 g/cm^3 , which corresponds to 93% of the theoretical density. In contrary the samples prepared with $\Phi = 7.7$ (i.e. LBCO1a, 1b, 1c) contain distinct, good observable crystalline domains, where the average grain size falls into the several hundred nm range (grains in the μm range are also presenting), see Fig. 7b and d. Indeed, latter samples exhibit high amount of pores, the geometrical densities vary between 4.7 and 4.4 g/cm^3 , which correspond to about 65% of the theoretical density. The reason for the limited grain growth of the samples prepared with $\Phi = 7.7$ is supposedly the different powder characteristics (e.g. average crystallite size) of the calcined powder samples. The LBCO1 sample

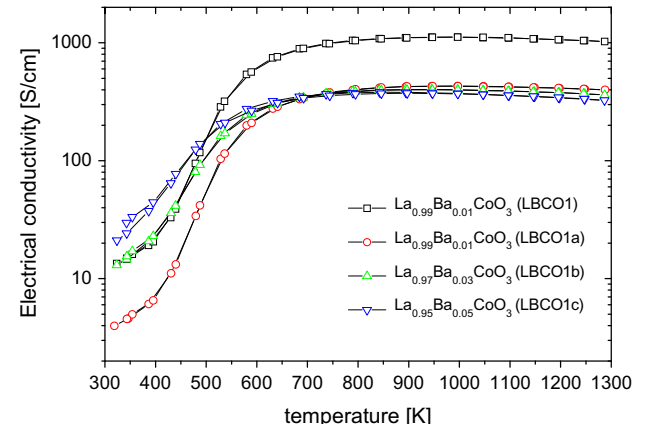


Fig. 8b. Temperature dependence of the electrical conductivity (σ) for the $\text{La}_{1-x}\text{Ba}_x\text{CoO}_3$ ($0.01 \leq x \leq 0.05$) samples.

consists of bigger crystallites has soft, light agglomerated powder characteristic, while LBCO1a, 1b, 1c powder samples have smaller sized, coarse-grained, highly agglomerated, rougher structure originating from the different burning characteristics by the gel combustion step.

In Fig. 8a the Seebeck coefficient is presented in the temperature range of 300–1300 K. All samples undergo transitions from a low temperature electrically insulating phase with high Seebeck coefficients to a high temperature insulating phase with improved electrical conductivities and lowered values of the Seebeck coefficients. The absolute values of the Seebeck coefficients are nearly identical for the two samples with 1% Ba^{2+} substitutions, while higher substitutions lead to a decrease of S ($T < 650 \text{ K}$) from $400 \mu\text{V/K}$ for 1% Ba^{2+} to $200 \mu\text{V/K}$ for 5% Ba^{2+} . This is to be expected because by the substitution with Ba^{2+} additional charge carriers are introduced, which lead to a decrease of Seebeck coefficient. In the

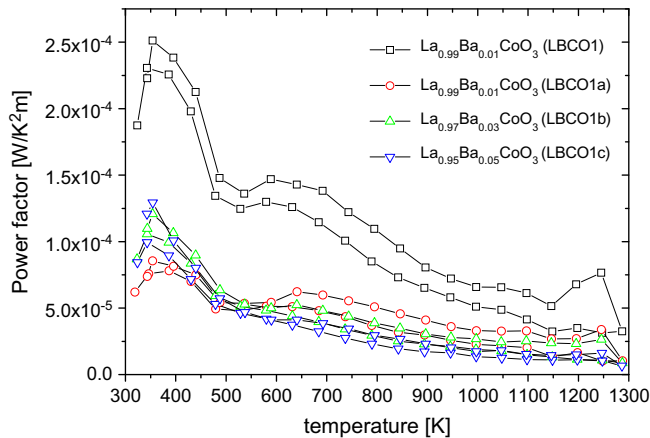


Fig. 8c. Temperature dependence of the calculated power factor values for the $\text{La}_{1-x}\text{Ba}_x\text{Co}_3$ ($0.01 \leq x \leq 0.05$) samples.

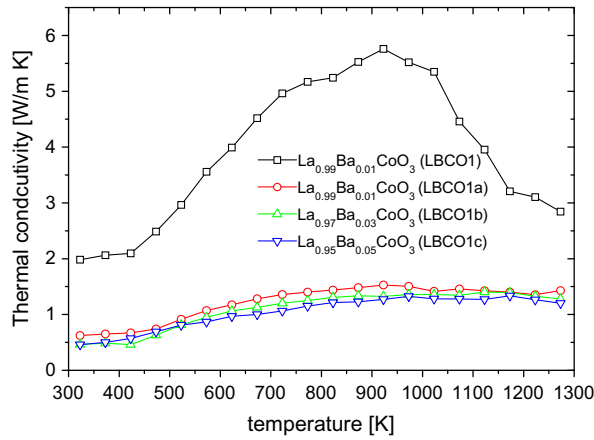


Fig. 9. Temperature dependent thermal conductivity (κ) of the $\text{La}_{1-x}\text{Ba}_x\text{Co}_3$ samples.

high temperature range ($T > 650$ K) the values of Seebeck coefficients are nearly temperature independent and similar for all samples with values around $25\text{--}30 \mu\text{V/K}$.

The metal insulator transition is confirmed by measurements of the electrical conductivity, which is shown in Fig. 8b. Here, sample LBCO1 prepared with $\Phi = 1.7$ at 1% Ba^{2+} substitution shows the highest conductivity. This is due to the highest relative density of this sample ($\rho_{\text{rel}} = 0.93$). At temperatures below 450 K the other samples with comparable densities show increasing conductivities with increasing amounts of Ba^{2+} . This finding is in line with an increase of carrier concentration by Ba^{2+} substitution. At higher temperatures the conductivities of all samples strongly increase more than one order of magnitude, becoming metallic at temperatures above 700 K.

In Fig. 8c the power factor of the samples as a function of temperature is illustrated. The power factor displays a decreasing characteristic for all samples. The LBCO1 sample shows far higher power factor than that of the other ones due to its higher density.

The temperature dependence of the thermal conductivity (κ) of LBCO samples can be seen in Fig. 9. LBCO1 sample reaches the highest thermal conductivity values because of its high compactness. Samples prepared with $\Phi = 7.7$ show much lower thermal conductivity (typically under 1.5 W/m K) which could originate from the increased number of grain boundaries (see Fig. 7b and d) and from the significant porosity in the sintered bodies, as well. In order to get better understanding of the origin of reduced thermal conductivity by the latter samples the measured κ values were

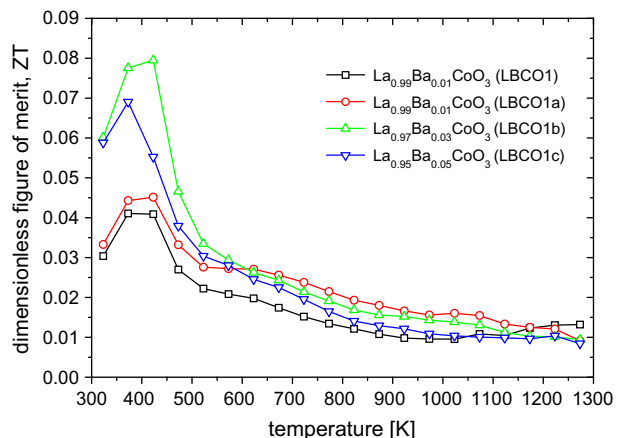


Fig. 10. Thermoelectric dimensionless figure-of-merit (ZT) of the LBCO samples in the 300–1300 K temperature range.

corrected with the calculated porosity of the sintered pellets. The corrected thermal conductivity to 100% density (κ_0) can be calculated by the following equation [34],

$$\kappa = \kappa_0(1 - P) \quad (1)$$

where κ is the measured thermal conductivity and P is the calculated porosity. It should be noted that Eq. (1) gives only a rough approximation for corrected thermal conductivity since the real pore structure, such as pore size distribution and pore morphology will be not taken into consideration. It follows from the above equation that the corrected κ_0 represents higher values with respect to the measured data. In Table 1 the measured thermal conductivity data at $T = 373$ K, the porosity and the corresponding corrected κ_0 values are presented. It can be concluded that the porosity corrected thermal conductivities for LBCO1a, 1b, 1c samples are about the half that of LBCO1. Supposedly, this could originate from the different microstructure (i.e. larger number of grain boundaries) of the sintered bodies. Regarding whether the measured κ or the corrected κ_0 , the values of the thermal conductivity of the samples with increasing Ba^{2+} content are comparable and the LBCO1c sample with the highest Ba^{2+} substitution (i.e. 5%) possesses the lowest κ value (taking into account the whole temperature range since a slight scattering of the measured data occurs in the lower temperature range). This phenomenon can be explained by mass disorder scattering of phonons, reducing the lattice part of the thermal conductivity.

Hereinbefore it has been demonstrated that the increased relative density (i.e. decreased porosity) of the sintered pellets results in higher thermal conductivity (see e.g. samples LBCO1 and LBCO1a), which has negative effect on ZT. However it can be assumed that electrical conductivity of the more porous samples (LBCO1a, 1b, 1c) would be further enhanced if more dense packing of the micron-sized grains would be achieved (e.g. due to optimizing sintering conditions or using other sintering techniques like spark plasma or microwave sintering). Hence, the improvement of the electrical conductivity due to lower porosity can exceed the efficiency loss due to increased thermal conductivity of the dense polycrystalline samples; consequently the overall ZT can be further improved. It can be seen in Fig. 8b that the extent of the electrical conductivity of the LBCO1a sample is about 50% of the LBCO1 sample, which could originate from the different microstructure (i.e. higher fraction of pores and larger number of grain boundaries). Note that, both samples contain nearly 1% Ba^{2+} , as it was controlled by EDX, as well (see Table 1). However, the major challenge by this approach is obtaining complete removal of any organics used in the wet chemistry processes, and obtaining as

close to 100% of theoretical density during compaction as possible. If this is not achieved, the carrier mobility will be substantially reduced by one or more orders of magnitude for just a few percent decrease in density [35] resulting in degraded ZT.

The sample with 3% Ba²⁺ substitution shows at lower temperature range a ZT value of 0.08, presented in Fig. 10. At higher temperatures all the samples become metallic and the corresponding diminution of Seebeck coefficient leads to a decrease of ZT.

4. Conclusion

Soft chemistry synthesis method was used to prepare highly crystalline single phase Ba²⁺ substituted cobaltate perovskite materials. During the gel formation and gel combustion no precipitation of insoluble Ba²⁺ species was observed which led to perovskite samples with high phase purity, proved by Rietveld refinement of the XRD data. The influence of fuel-to-oxidizer ratio (Φ) on the microstructure of the calcined powder, as well as of the sintered pellets was investigated. It was found that Φ has crucial role on the powder microstructure and on sinterability, consequently on the characteristics of the sintered pellet. Consolidation of the powder samples results in sintered bodies with different microstructures depending on the initial powder character. This is due to different burning characteristics of the polymeric gels during combustion. LBCO samples prepared with higher Φ exhibit coarse grained structure in contrast to a finer, light agglomerated powder structure obtained at lower Φ . Thermoelectric transport property measurement showed that all samples undergo transitions from a low temperature insulating phase (high S) to a high temperature insulating phase (low S). The electrical and thermal conductivity showed strong dependence on the microstructure. Increasing Ba²⁺ substitution lowered the thermal conductivity values, which was due to mass disorder scattering of phonons. It was further concluded that thermal conductivity could be minimized by using coarse grained powder samples and electrical conductivity could be improved by optimization of the sintering procedure. The calculated dimensionless figure-of-merit (ZT) showed maximum value for La_{0.97}Ba_{0.03}CoO₃ at about 400 K of ZT \sim 0.08.

Acknowledgements

This work was supported by the State and University of Bremen in the framework of the Integrated Solutions in Sensorial Structure Engineering (ISIS), Fund No. 54 416 911. The authors would like to thank the thermoanalytical measurements for Ádám Juhász and Prof. Imre Dékány at University of Szeged, Hungary.

References

- [1] R. Robert, S. Romer, A. Reller, A. Weidenkaff, Nanostructured complex cobalt oxides as potential materials for solar thermoelectric power generators, *Adv. Eng. Mater.* 7 (2005) 303–308.
- [2] W. Liu, X. Yan, G. Chen, Z. Ren, Recent advances in thermoelectric nanocomposites, *Nano Energy* 1 (2012) 42–56.
- [3] J.R. Szczech, J.M. Higgins, S. Jin, Enhancement of the thermoelectric properties in nanoscale and nanostructured materials, *J. Mater. Chem.* 21 (2011) 4037–4055.
- [4] D.L. Medlin, G.J. Snyder, Interfaces in bulk thermoelectric materials: a review for current opinion in colloid and interface science, *Curr. Op. Colloid Interface Sci.* 14 (2009) 226–235.
- [5] R. Robert, M.H. Aguirre, P. Hug, A. Reller, A. Weidenkaff, High-temperature thermoelectric properties of Ln(Co, Ni)O₃ (Ln=La, Pr, Nd, Sm, Gd and Dy) compounds, *Acta Mater.* 55 (2007) 4695–4972.
- [6] K. Muta, Y. Kobayashi, K. Asai, Magnetic, electronic transport, and calorimetric investigations of La_{1-x}Ca_xCoO₃ in comparison with La_{1-x}Sr_xCoO₃, *J. Phys. Soc. Jpn.* 71 (2002) 2784–2791.
- [7] H. Masuda, T. Fujita, T. Miyashita, M. Soda, Y. Yasui, Y. Kobayashi, M. Sato, Transport and Magnetic Properties of R_{1-x}A_xCoO₃ (R=La, Pr and Nd; A=Ba, Sr and Ca), *J. Phys. Soc. Jpn.* 72 (2003) 873–878.
- [8] M.S. Khalil, Synthesis, X-ray, infrared spectra and electrical conductivity of La/Ba-CoO₃ systems, *Mater. Sci. Eng. A* 352 (2003) 64–70.
- [9] S.B. Patil, H.V. Keer, D.K. Chakrabarty, Structural, electrical, and magnetic properties in the system Ba_xLa_{1-x}CoO₃, *Phys. Stat. Sol.* 52 (1979) 681–686.
- [10] P. Mandal, P. Choudhury, S.K. Biswas, B. Gosh, Transport and magnetic properties of La_{1-x}Ba_xCoO₃, *Phys. Rev.* 70 (2004) 104407.
- [11] S. Cizauskaite, S. Johnsen, J.E. Joergensen, A. Kareiva, Sol-gel preparation and characterization of non-substituted and Sr-substituted gadolinium cobaltates, *Mater. Chem. Phys.* 125 (2011) 469–473.
- [12] J. Androulakis, P. Migiakis, J. Giapintzakis, La_{0.95}Sr_{0.05}CoO₃: an efficient room-temperature thermoelectric oxide, *Appl. Phys. Lett.* 84 (2004) 1099–1101.
- [13] D.S. Melo, E.P. Marinho, L.E.B. Soledade, D.M.A. Melo, S.J.G. Lima, E. Longo, I.M.G. Santos, A.G. Souza, Lanthanum-based perovskites obtained by the polymeric precursor method, *J. Mater. Sci.* 43 (2008) 551–556.
- [14] C. Singh, M. Rakes, Preparation and characterization of nickel doped, A and B site LaCoO₃ perovskite, *Ind. J. Eng. Mater. Sci.* 16 (2009) 288–290.
- [15] Z. Junwu, S. Xiaojie, W. Yanping, W. Xin, Y. Xujie, L. Lude, Solution-phase synthesis and characterization of perovskite LaCoO₃ nanocrystals via a co-precipitation route, *J. Rare Earths* 25 (2007) 601–604.
- [16] A. Weidenkaff, Preparation and application of nanostructured perovskite phases, *Adv. Eng. Mater.* 6 (2004) 709–714.
- [17] E. Pál, V. Hornek, A. Oszkó, I. Dékány, Hydrothermal synthesis of prism-like and flower-like ZnO and indium-doped ZnO structures, *Coll. Surf. A: Physicochem. Eng. Aspects* 340 (2009) 1–9.
- [18] H.B. Park, H.J. Kweon, Y.S. Hong, S.J. Kim, K. Kim, Preparation of La_{1-x}Sr_xMnO₃ powders by combustion of poly(ethylene glycol)-metal nitrate gel precursors, *J. Mater. Sci.* 32 (1997) 57–65.
- [19] K.V. Rao, C.S. Sunandana, Co₃O₄ nanoparticles by chemical combustion: Effect of fuel to oxidizer ratio on structure, microstructure and EPR, *Solid State Commun.* 148 (2008) 32–37.
- [20] S.R. Nair, R.D. Purohit, A.K. Tyagi, P.K. Sinha, B.P. Sharma, Role of glycine-to-nitrate ratio in influencing the powder characteristics of La(Ca)CrO₃, *Mater. Res. Bull.* 43 (2008) 1573–1582.
- [21] L. Predoana, B. Malic, M. Zaharescu, LaCoO₃ formation from precursors obtained by water-based sol-gel method with citric acid, *J. Therm. Anal. Calorim.* 98 (2009) 361–366.
- [22] R. Kun, J.H. Fendler, Use of attenuated total internal reflection fourier transform infrared spectroscopy to investigate the adsorption of and interactions between charged latex particles, *J. Phys. Chem. B* 108 (2004) 3462–3468.
- [23] P. Smitha, P.K. Pandey, N.S. Gajbhiye, Polyol based auto-combustion synthesis of nanostructured PZT and its characterization, *Mater. Chem. Phys.* 109 (2008) 500–505.
- [24] S. Nakayama, M. Okazaki, Y.L. Aung, M. Sakamoto, Preparations of perovskite-type oxides LaCoO₃ from three different methods and their evaluation by homogeneity, sinterability and conductivity, *Solid State Ionics* 158 (2003) 133–139.
- [25] D. Berger, C. Matei, F. Papa, G. Voicu, V. Fruth, Pure and doped lanthanum cobaltites obtained by combustion method, *Prog. Solid State Chem.* 35 (2007) 183–191.
- [26] J. Qiu, H. Fan, X. Zheng, Pb(Zr_{0.95}Ti_{0.05})O₃ powders synthesized by Pechini method: Effect of molecular weight of polyester on the phase and morphology, *J. Sol.-Gel, Sci. Technol.* 42 (2007) 21–26.
- [27] P.M. Raccah, J.B. Goodenough, First-Order Localized-Electron \leftrightarrow Collective-Electron Transition in LaCoO₃, *Phys. Rev.* 155 (1967) 932–943.
- [28] G. Thornton, B.C. Tofield, D.E. Williams, Spin state equilibria and the semiconductor to metal transition of LaCoO₃, *Solid State Commun.* 44 (1982) 1213–1216.
- [29] G. Thornton, B.C. Tofield, A.W. Hewat, A neutron diffraction study of LaCoO₃ in the temperature range 4.2 $< T <$ 1248 K, *J. Solid State Chem.* 61 (1986) 301–307.
- [30] M.B. Bellakki, J. Das, V. Manivannan, Synthesis, and measurement of structural and magnetic properties, of La_{1-x}Cd_xCoO₃ perovskite ceramic oxides, *J. Electroceram.* 24 (2010) 319–325.
- [31] R. Robert, D. Logvinovich, M.H. Aguirre, S.G. Ebbinghaus, L. Bocher, P. Tomeš, A. Weidenkaff, Crystal structure, morphology and physical properties of LaCo_{1-x}Ti_xO_{3±δ} perovskites prepared by a citric acid assisted soft chemistry synthesis, *Acta Mater.* 58 (2010) 680–691.
- [32] R.D. Shannon, Revised effective ionic radii and systematic studies of interatomic distances in halides and chalcogenides, *Acta Cryst. A* 32 (1976) 751–767.
- [33] H. Ullmann, N. Trofimienko, F. Tietz, D. Stöver, A. Ahmad-Khanlou, Correlation between thermal expansion and oxide ion transport in mixed conducting perovskite-type oxides for SOFC cathodes, *Solid State Ionics* 138 (2000) 79–90.
- [34] T. Nozaki, K. Hayashi, T. Kajitani, Mn-substitution effect on thermal conductivity of delafossite-type oxide CuFeO₂, *J. Electron. Mater.* 39 (2010) 1798–1802.
- [35] C.J. Vineis, A. Shakouri, A. Majumdar, M.G. Kanatzidis, Nanostructured thermoelectrics: big efficiency gains from small features, *Adv. Mater.* 22 (2010) 3970–3980.